Atomic-scale control of TiO$_6$ octahedra through solution chemistry towards giant dielectric response

Wanbiao Hu[1,2], Liping Li[1], Guangshe Li[1], Yun Liu[2] & Ray L. Withers[2]

[1]State Key Laboratory of Structural Chemistry, Fujian Institute of Research on the Structure of Matter, Chinese Academy of Sciences, Fuzhou 350002, P. R. China, [2]Research School of Chemistry, The Australian National University, ACT 0200, Australia.

The structures of many important functional oxides contain networks of metal-oxygen polyhedral units *i.e.* MO_n. The correlation between the configurations and connectivities of these MO_n to properties is essentially important to be well established to conduct the design, synthesis and application of new MO_n-based functional materials. In this paper, we report on an atomic-scale solution-chemistry approach that for the first time enables TiO$_6$ octahedral network control starting from metastable brookite TiO$_2$ through simultaneously tuning pH values and interfering ions (Fe^{3+}, Sc^{3+}, and Sm^{3+}). The relationship between solution chemistry and the resultant configuration/connectivity of TiO$_6$ octahedra in TiO$_2$ and lepidocrocite titanate is mapped out. Apart from differing crystalline phases and morphologies, atomic-scale TiO$_6$ octahedral control also endows numerous defect dipoles for giant dielectric responses. The structural and property evolutions are well interpreted by the associated H$^+$/OH$^-$ species in solution and/or defect states associated with Fe^{3+} occupation within TiO$_6$ octahedra. This work therefore provides fundamental new insights into controlling TiO$_6$ octahedral arrangement essential for atomic-scale structure-property design.

The crystal structures and functional properties of metal oxide materials are directly affected by the arrangement of their constituent MO_n polyhedral building blocks[1,2]. Atomic-scale control over these arrangements is extremely important because **1**: controlling the way to link MO_n polyhedra together favors the creation of novel nanostructures, with a wide variety of particle sizes, crystal structures and morphologies[3]; **2**: control of the local distortions and defect chemistry of the constituent MO_n polyhedra can alter electrical properties such as local dipole moments and macroscopic polarization[4]; and **3**: both the individual MO_n configurations and their connectivities can profoundly affect the growth kinetics of metal oxides. Reliable control of the above factors enables the design of new solid-state materials and the associated development of novel practical applications.

TiO$_6$-octahedral-based functional materials, *e.g.* several typical Ti-containing oxides (TiO$_2$ and layer-structured titanates), exhibit versatile properties *e.g.* photovoltaic, electrochemical, catalytic and dielectric properties[5–8]. These functional oxides are built of the same fundamental TiO$_6$ polyhedral building units (see *e.g.* Figure 1a) but connected differently[9]. The gaining of the necessary control over the local TiO$_6$ octahedral arrangement is essential for property tailoring. Although a multitude of efforts have been devoted, the usual synthesis routes do not allow simultaneous control over structural/phase evolution, defect chemistry and resultant properties of the materials produced[10]. Otherwise, the synthetic strategies have to involve extremely complicated procedures and/or insurmountable challenges arising from using capping complexes that invariably either obscure the desired structural configurations or undermine surface reactivity. To date, only a few examples (mainly perovskites) refer to TiO$_6$ octahedral tilting, rotating and/or distortions[2], which are only fabricated in non-solution ways, and what's more, these have to be subject to thermally/dynamically nonequilibrium states *e.g. via* sintering under high temperatures/pressures[11], or based on external strains/stimulus[12], or forming local intergrowth with non-stoichiometry[13]. As such, the control of TiO$_6$ octahedral arrangements from equilibrium-state solution chemistries, *i.e.* the connectivities and configurations thereto on the atomic-scale level, remains unsuccessful. As a result, an investigation on TiO$_6$ octahedral evolutions and the relationships between TiO$_6$ octahedral arrangements and the resultant structures/properties is still missing.

There remains an urgent and ongoing need for new synthetic strategies enabling control over TiO$_6$ octahedral configurations and connectivities. To this end, we herein report on a new, facile solution-chemistry approach with which the relationship between the synthesis variables and the resultant TiO$_6$ octahedral networks is mapped out
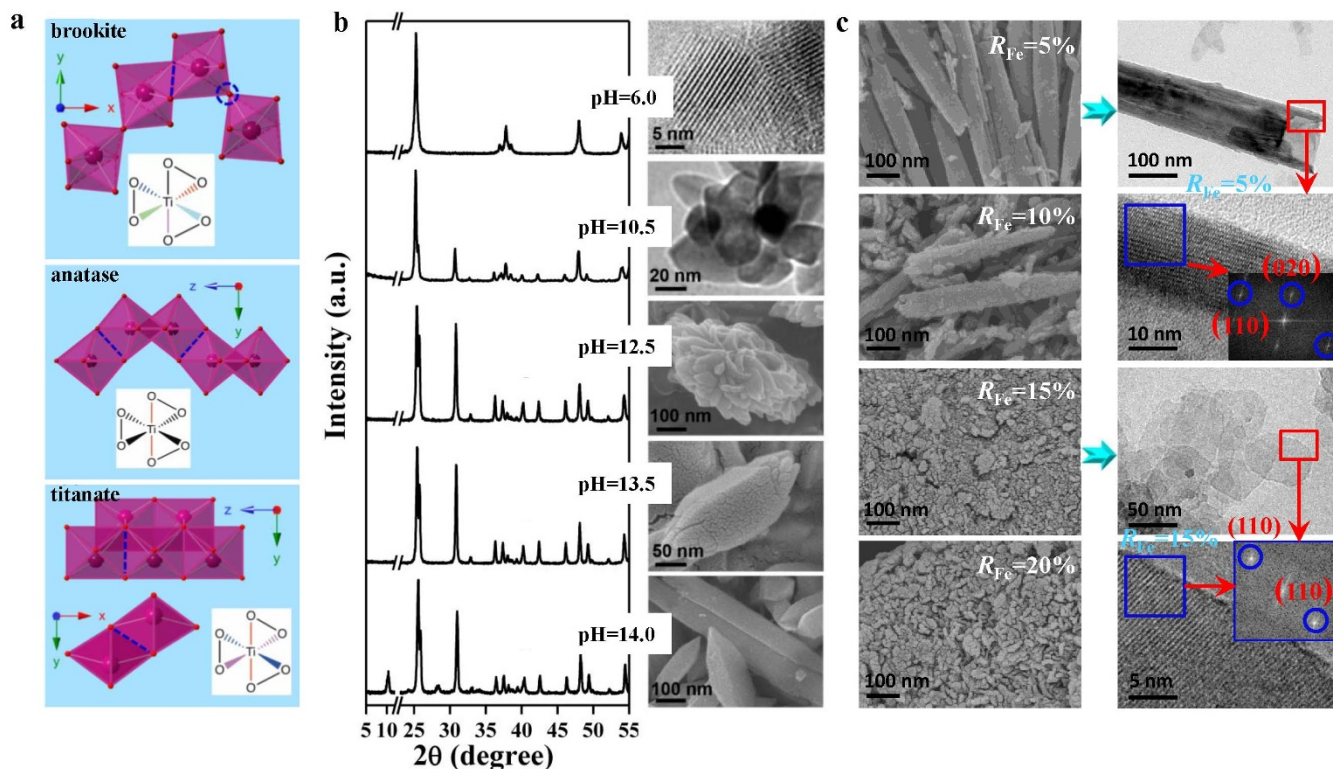
Figure 1 | Representations of the connectivity and configurations of TiO$_6$ octahedra, and their control under solution reaction conditions allowing crystalline phase and morphology evolutions in TiO$_2$ and layer-structured Lepidocrocite-type titanate. (a) The connectivity and configurations of TiO$_6$ octahedra in brookite, anatase and lepidocrocite-type titanate. The arrows denote the axial directions (*e.g. x, y,* and *z*) of the crystal structure. The blue dashed lines and circles denote edge-sharing and vertex/corner-sharing connections, respectively. The white frames demonstrate the configurations in a TiO$_6$ octahedron corresponding to respective structures, where the same (different) colors mean the same (different) length of Ti–O bonds. (b) TiO$_6$ octahedral modification through pH controlling giving rise to the structural evolution (XRD patterns, and SEM/TEM images). (c) SEM (left: R_{Fe} = 5%–20%) and TEM/HRTEM (right: R_{Fe} = 5% and 15%) images of as-prepared lepidocrocite-type titanate for the TiO$_6$ octahedral modification controlled through the introduction of interfering (Fe^{3+}) ions. Inset in c-right are the Fourier-transform diffraction patterns corresponding to the HRTEM.

in terms of controlling simultaneously the pH values of solutions and interfering/blocking ions (Fe^{3+}, Sc^{3+}, and Sm^{3+}). On the one hand, the interaction between H$^+$/OH$^-$ groups and TiO$_6$ octahedral networks could respond to a strong negative/positive voltage and exhibit a large increase in electrical capacitance and subsequent variation in TiO$_6$ octahedral arrangements[14]. The kinetics of nucleation/growth in solutions can thus be manipulated[15], as theoretically predicted[16], by the presence of H$^+$/OH$^-$ species since they influence the surface energies and surface tension, leading to variations in morphology and phase stability of TiO$_2$. On the other hand, interfering/blocking ions could permit the local environment of the TiO$_6$ octahedra to be altered[17], introduce local chemical defects and change the local chemical potential energy of the particular TiO$_6$ octahedra involved[10,18]. Likewise, introducing interfering ions could probably cause local distortion, even breaking the local symmetry of the TiO$_6$ octahedra, giving rise to new local polarization states.

In the light of the two synthetic variables for tuning TiO$_6$ octahedral configurations and connectivities described above, this paper presents the atomic-scale control of TiO$_6$ octahedra in several typical titanium-containing oxides (*e.g.* TiO$_2$ and layer-structured lepidocrocite-type titanate) from solutions and builds the correlation between TiO$_6$ octahedral control and structures/properties.

Results

Like many other functional titanium-containing oxides, TiO$_2$ (anatase, brookite and rutile) and titanates are all built out of the same basic structural unit, TiO$_6$ octahedron. Figure 1a shows the arrange-

ments of TiO$_6$ octahedra in brookite, anatase and lepidocrocite-type titanate, showing distinctly different TiO$_6$ octahedral configurations (*i.e.*, different Ti–O bond lengths and angles) and connectivities (*i.e.*, edge-sharing and vertex/corner-sharing connections). Depending on the local arrangements of TiO$_6$ octahedra, the resultant oxides have different crystal structures. This can be considerably influenced by the reaction parameters, solution pH and the concentration of interfering ions, during the solution synthesis.

TiO$_6$ octahedral connectivity and configurations controlled through pH tuning. The connectivity types as well as the local configurations of the individual TiO$_6$ octahedra are strongly influenced by pH value (pH = 1 ~ 14) without interfering ions. Thereby, as a result of the TiO$_6$ octahedral control under different pH conditions, the corresponding crystalline nanophases, morphologies/microstructures show considerable diversity (Figure 1b). The reaction condition of pH ≤ 6.0 usually gives anatase TiO$_2$ nanophases (Figures 1b, S1) with edge-sharing connectivity of TiO$_6$ octahedra (Figure 1a). The average crystallite sizes of the resultant compounds are estimated to be between 8.2 nm (pH = 1) and 21 nm (pH = 6) from the strongest diffraction line (101) for anatase using Scherrer equation, consistent with TEM result. It is interesting that rutile TiO$_2$ seems able to exist only with pH range of 2.0–3.0 (S1). A high pH value, by contrast, promotes vertex-sharing connectivity of the TiO$_6$ octahedra (Figure 1a) as evidenced by the appearance of brookite phase (Figure 1b) particularly with pH value of 10.5, which still gives a mixture of spindle-shaped brookite, and square-like anatase phases. Pure brookite phase was achieved when pH value is varied

between 12.0 and 14.0, as confirmed by the structural refinements (S2–S4). While, the resultant morphologies are highly pH-sensitive, *i.e.*, flower-shaped assemblies with a dimension of ~2 μm at pH = 12.5 and well-dispersed spindle-shaped brookite particles with dimensions around 300 nm along the axial direction and 100 nm along the cross-sectional direction at pH = 13.5. When the pH value is beyond 14.0, a new secondary phase with the strongest diffraction at $2\theta = 9.8°$ appears in addition to the dominant brookite phase (Figure 1b and S5), presenting two different morphologies: spindle-shaped brookite and rod-like layered titanates with scrolled TiO_6 frameworks. This new phase is related to a type of sodium-containing titanate (EDS in S5) that has a corner/edge-sharing TiO_6 octahedral connectivity (Figure 1a)[19]. Upon further increase of the alkalinity (OH^-), brookite is always the major phase unless extremely high alkali conditions such as the (OH^-) concentration 5 M reported for lepidocrocite-type titanate nanotubes (TNTs)[20]. Unfortunately, such an extremely high alkalinity would not be favorable to control the TiO_6 octahedral units, nor the size, morphology, and chemical compositions of the final products.

It is noted that only a few papers to date report obtaining pure brookite TiO_2. Usually, it coexists easily with anatase, implying the difficulty in the formation of pure brookite TiO_2 phase[21,22]. Even in this work, pure brookite TiO_2 is limited to a relatively narrow pH value range. For this reason, the subsequent control over the configurations and connectivity of TiO_6 octahedra using interfering ions will be based on high-purity brookite. As a matter of fact, all the nanophases/structures can be achieved by changing synthesis conditions from the starting brookite TiO_2, so we note here that the controlling process can be generally considered as a process of TiO_6 octahedral modification.

TiO_6 octahedral connectivity and configurations controlled through the interfering ions.

Dominant nanophase evolution. The introduction of interfering Fe^{3+} ions at pH = 12.5 leads to a nanophase transformation from brookite to anatase and/or lepidocrocite-type titanate, *i.e.* the TiO_6 octahedra were modified. Pure-phase brookite was obtained when pH = 12.5 without interfering Fe^{3+} ion, while a small amount of Fe^{3+} ions, *e.g.* R_{Fe} = 5%, results in anatase TiO_2 formation (S6 and S7), which is confirmed by the decreased intensity of the (121) to the (120) peak (see the detailed explanation in Figure S8), the appearance of a Raman peak at 515 cm^{-1} (S8) corresponding to anatase[23], also the inhomogeneous morphologies observed (S7). The ratio of the brookite to the anatase phase is about 79: 21 in this specific case, estimated via XRD refinement (S9). When the R_{Fe} increases up to or beyond 10%, the TiO_6 octahedral configuration and connectivity are mainly of lepidocrocite-type titanate form rather than anatase, suggesting that interfering Fe^{3+} ion favors the former. It is apparent that the interfering Fe^{3+} ion behavior differs by contrast with previous work where Fe^{3+} ions may either be stably doped into the anatase/rutile phase[17,18], or a transformation from anatase to rutile was deduced[10]. Most importantly, the interfering ions seem to be dispatched into lepidocrocite-type titanate rather than remaining in brookite (S10).

As discussed above, interfering Fe^{3+} ions play an important, but still limited, role in the control of TiO_6 octahedral configurations and connectivity for pH ≤ 12.5 because (i) both brookite and lepidocrocite-type titanate phases always coexist even at R_{Fe} = 20% (S6) and (ii) the morphologies were different due to the two-phase coexistence (S7). However, if the pH value is increased slightly up to 13.5, only a small amount of interfering Fe^{3+} ions (*e.g.*, R_{Fe} = 5%) is required to achieve pure-phase sodium-containing titanate (clearly indicated by XRD (S11), and EDS (S12)) without a trace of either the brookite or anatase phase. Pure-phase lepidocrocite-type titanate can always be achieved over a broad Fe^{3+} amount range of R_{Fe} = 5–20% (S11). Note that without interfering Fe^{3+} ions, it is impossible to form the

lepidocrocite-type titanate. Further increasing the pH value, *e.g.* beyond pH = 14, however, is not suitable for the control of TiO_6 octahedral configurations and connectivity as the Fe^{3+} no longer behaves like an interfering ion as described above, instead forming iron-based oxide phases (S13).

Dominant microstructure evolution. Apart from the control of the connectivity and configurations of TiO_6 octahedral units to achieve lepidocrocite-type titanate nanophases, the interfering Fe^{3+} ions also lead to macro/microscopic morphological and structural evolution. The SEM/TEM images (Figure 1c) demonstrate a distinct transformation in morphology from tubular structures to sheet-like nanoparticles with increasing R_{Fe}. Relatively low R_{Fe} (*e.g.* 5%) advances the formation and further rearrangement of distorted and scrolled TiO_6 octahedral frameworks to form lepidocrocite-type titanate tubular structures. A typical tube possesses inner/outer diameter of around 50/120 nm, and a length of up to several microns. These tubes are apparently different from those titanate nanotubes (TNTs) reported previously that were characterized by scrolling-up of 3–4 layered structures with inner/outer diameter of several/tens nanometers[24]. The resultant tubes in this work are highly crystallized with lattice spacings of 0.362 nm and 0.669 nm, corresponding to the (110) and (020) planes of the lepidocrocite-type titanates (Figure 1c-inset). Although TNTs have been well explored under concentrated alkali conditions (*e.g.*, 10 M NaOH)[24], we have not seen any report with respect to such titanate tubes to date, especially obtained with such a lower pH value.

After the intermediate stage where the lepidocrocite-type titanates show a mixture of short rod-like and round particles (*e.g.*, R_{Fe} = 10%), the lepidocrocite-type titanate tubes are completely transformed into small-scale nanosheets when the R_{Fe} increases up to 15% (Figure 1c). These nanosheets are ~50 nm in the two-dimensional plane and highly crystallized with a *d* value of 0.362 nm that belongs to the (110) plane. Such a sheet-like morphology remains unchanged even when R_{Fe} reaches 20% (Figure 1c). We note that utilization of other interfering ions with different sizes (or charges) may greatly influence the resulting structures such as the cases of Sc^{3+} (S14) and Sm^{3+} (S15), 5% of which could form pure-phase lepidocrocite titanate with nanosheet shapes.

Microstructure identification. To examine the crystalline structures and locally TiO_6 octahedral variations, spectroscopic techniques were used. For Raman, nine vibrations (Figure 2a) for all titanates were detected around 187, 279, 387, 442, 567, 663, 703, 785, and 906 cm^{-1}, which match fairly well the structure with the orthorhombic layered lepidocrocite titanate (Figures 1a, 3b), a type of protonic acid $H_{2-x}Ti_{2-x/4}\square_{x/4}O_4$ ($\square$: vacancy)[19,20]. Nonetheless, the lengths of the Ti–O bonds and the symmetry of the corresponding octahedra are greatly changed, as indicated by apparent Raman shifts towards lower wavenumbers at 442 and 703 cm^{-1}. The Raman band at 663 cm^{-1}, with the same origin as the A_g mode of 703 cm^{-1}, is associated with the bending of TiO_6 octahedral layers during the formation of lepidocrocite-type titanates via scrolling of Ti–O networks[25]. With increasing R_{Fe}, this band gradually disappears, reflecting the transformation from titanate tubes to nanosheets. Systematic shift of Ti–O vibrations with increasing R_{Fe} is also reflected by FT-IR spectra (Figure 2b), *e.g.*, a Ti–O vibration shifting from 679 to 657 cm^{-1}. While, the vibration of interlayered Ti–O–Na bonds[19] at 899 cm^{-1} does not show any shifts with increasing the R_{Fe} but only weakens gradually, indicating that a small amount of Fe^{3+} would be dispatched to the interlayer sites to occupy the original Na^+ locations. EPR (Figure 2c, a detailed EPR is also see Figure S16) signal of g_{eff} = 4.3, a characteristic of isolated Fe^{3+} ions, is related to Fe^{3+} cations into an orthorhombic structure. Its decrease indicates that the diffusion of Fe^{3+} ions is progressed from their initial location at the oxide lattice towards the surface/interface/interlayer[18]. Consequently, gradual weakening of this signal also implies that a
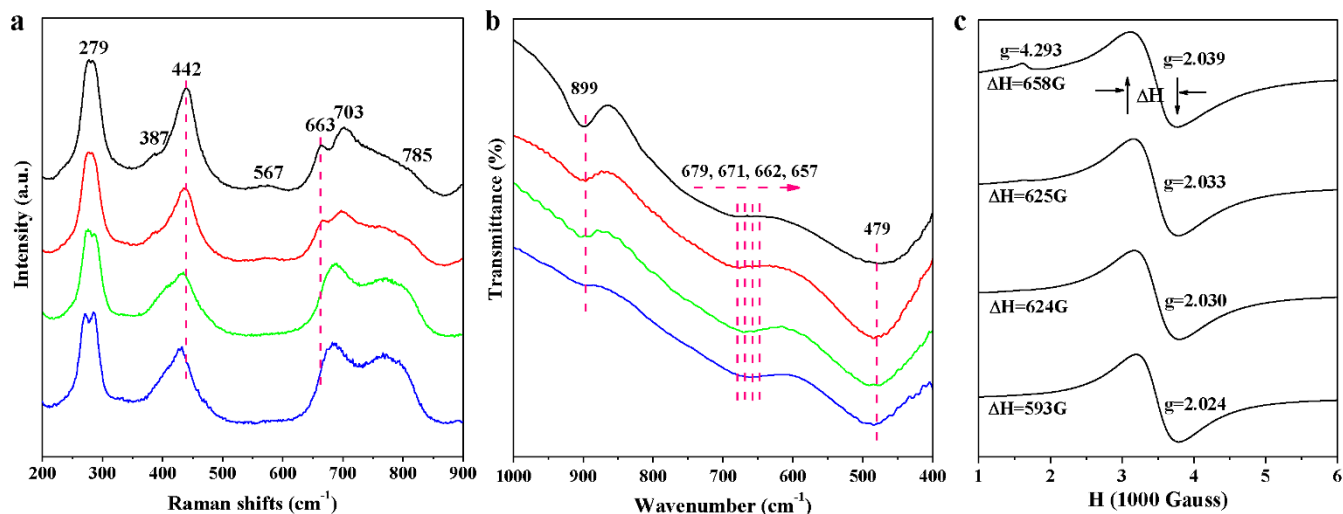
Figure 2 | Spectroscopic characterizations of lepidocrocite-type titanates with varying R_{Fe}. (a) Raman spectra. (b) Furrier-Transition infrared (FT-IR) spectra. (c) Electron paramagnetic resonance (EPR) spectra. The curve from top to bottom denotes the spectrum of R_{Fe} = 5%, 10%, 15%, 20%, respectively.

part of dopant Fe^{3+} ions was transported to the interlayered sites as those Fe^{3+} doped tetra-titanate bulks ($K_2Ti_4O_9$), where Fe^{3+} ions occupy the sites of interlayered K^+ ions[26].

For layered lepidocrocite titanate, a predominant characteristic is that interlayer ions are exchangeable with a variety of inorganic cations or organic groups[27]. One may thus assume that interlayer spaces can accommodate Na^+ and/or H^+ to compensate the charge neutralization. In terms of TG-DTG analysis (Figures 3a, S17), all the lepidocrocite-type titanates followed a similar three-fold dehydration process. For instance, the titanate formed at R_{Fe} = 15% loses 13 wt% of its total weight due to the dehydration of physisorbed water at 106°C, of chemisorbed water at 169°C and of interlayer protons at ~206°C, corresponding to weight losses of 5.4 wt%, 2.4 wt%, and 5.2 wt%, respectively. Furthermore, ICP-AES measurement (Table S1) suggests the molar ratio of Fe to Ti coincides with their initial nominal ratios. With increasing R_{Fe}, the numbers of interlayer protons increased, accompanied by a slight decrease in

the molar ratio of Na to (Fe+Ti) when R_{Fe} is beyond 15%. This, consistent with FT-IR and EPR, confirms that a small amount of Fe^{3+} dopants are probably dispatched into the interlayer Na^+ sites. As a result, the structural components of the present lepidocrocite-type titanate can be expressed by the general formula $H_xNa_yTi_{2-z}Fe_m\square_nO_4 \cdot rH_2O$ ($\square$ = vacancy), where the Na^+ ions and/or protons (H^+ or $[H_3O]^+$) or even Fe^{3+} cations co-occupy the inter-layer regions between the main framework of the TiO_6 octahedra, as schematically shown in Figure 3b.

Mapping TiO_6 octahedral connectivity and configurations under solutions for tunable nanophases and nanostructures. To achieve a comprehensive understanding of how to control the configurations and connectivities of TiO_6 octahedra, experiments under a broad range of pH conditions in conjunction with a given R_{Fe} were performed, giving rise to tunable nanophases and nanostructures. When fixing R_{Fe} = 5%, solution reaction with a high alkalinity (pH =
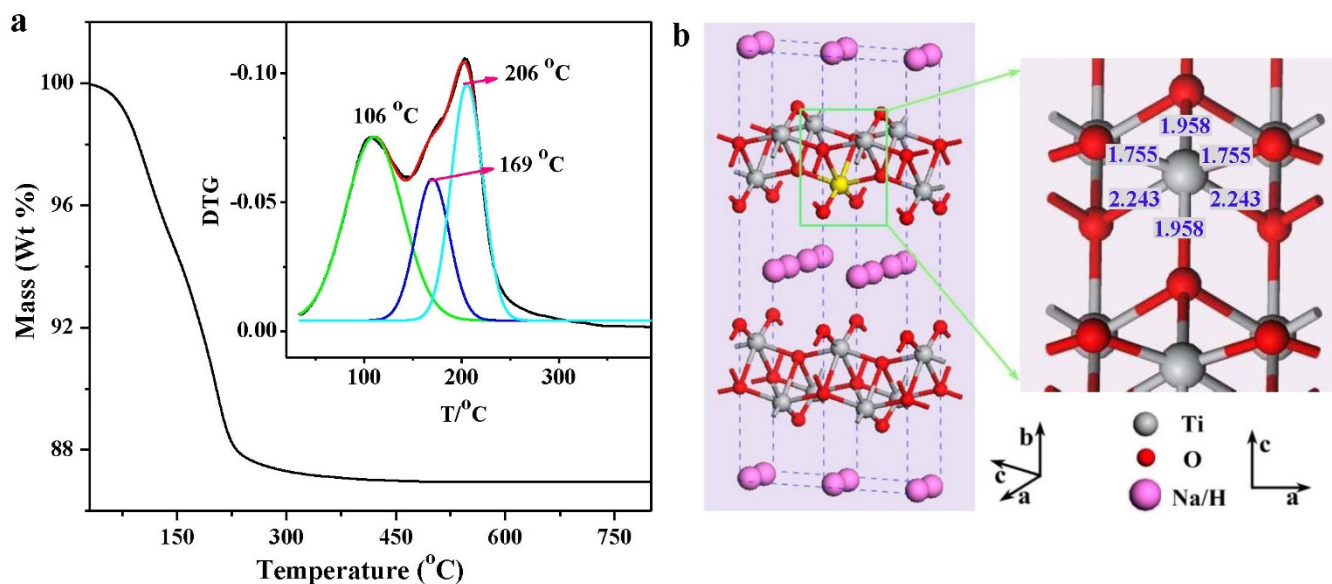

Figure 3 | (a) Thermogravimetric (TG) and (b) Crystal structure of lepidocrocite-type titanate. a-inset is the differentiated TG (DTG) curve (black) of R_{Fe} = 15% and fitting results (colored). b-right shows the chemical coordination of TiO_6 octahedron where the numbers denote the lengths (unit: Å) of Ti-O bonds.
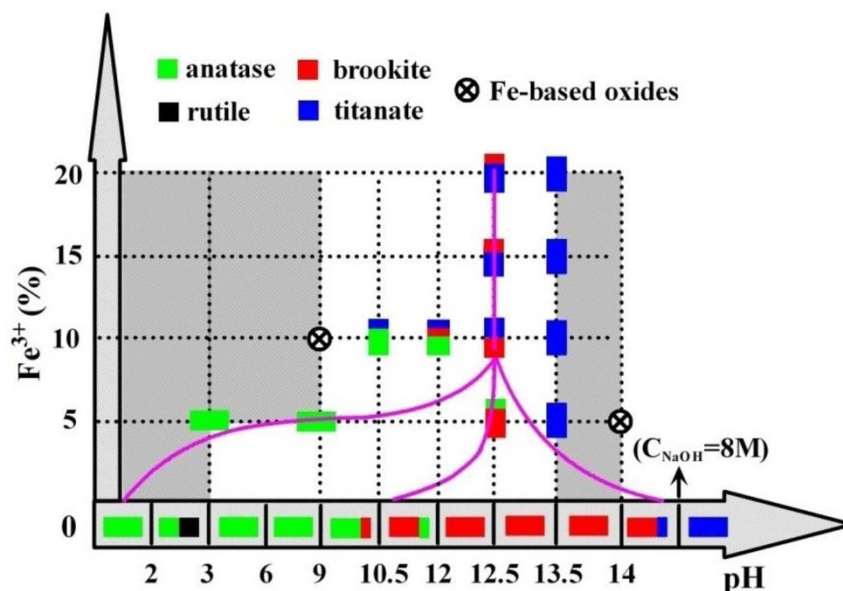
Figure 4 | **Map of TiO$_6$ octahedral modification through simultaneously controlling over the solution pH values and doping levels of interfering Fe^{3+} ions.**

14) leads to the occurrence of α-Fe$_2$O$_3$. While, low pH conditions (pH < 3.0) generally caused a significant loss of Fe^{3+} because of high solvency. A single-phase Fe^{3+} doped anatase would therefore form in the conditions of either weak alkalinity (pH = 9.0) or acidity (pH = 3.0). The pH values in between (S13) that, indeed, are the optimum pH conditions for growing Fe^{3+} doped anatase TiO$_2$ nanocrystals[28].

Once R_{Fe} reached 10%, a relatively high alkalinity leads to the coexistence of two (pH = 12.0) or three nano-phases (pH = 10.5) like anatase, titanate and brookite (S18). Nevertheless, the Fe-based oxide, e.g. α-Fe$_2$O$_3$, also appears even at a weak alkalinity of pH = 9.0, meaning that a high R_{Fe} and a relatively low pH value cause the formation of Fe-based oxides. A map outlining the nanophases and nanostructure evolution achieved is shown in Figure 4. This map provides a feasible and controllable route for the configurations and connectivity of TiO$_6$ octahedral units controlled via pH values and Fe^{3+} dopant concentrations.

Effect of the structural evolutions on the giant dielectric responses. Giant dielectric permittivities (ε') of ~10^4 were obtained at room temperature for all the lepidocrocite-type titanates (Figure 5a): ε' decreases with increasing frequency and then turns flat in the higher frequency range. With increasing R_{Fe}, the lepidocrocite-type titanate shows a higher and frequency-independent ε'. Most strikingly, the titanate with R_{Fe} = 15% showed a ε' of larger than 10^4 over a wide frequency range up to 10^5 Hz. Beyond R_{Fe} = 15%, the dielectric permittivity drops to a lower level with the fall threshold value at a relatively lower frequency. All titanates exhibit a similar Debye-like relaxation feature in ε'' curves[29]. This relaxation peak shifts towards the higher frequencies with increasing R_{Fe}, reaching a maximum value of 76.2 kHz for R_{Fe} = 15%. Afterwards, the peak, for the lepidocrocite-type titanate with R_{Fe} = 20%, shifts slightly towards lower frequency. The relaxation time (τ) is also estimated to be 395, 64, 4.2, and 9.4 μs for the lepidocrocite-type titanates of R_{Fe} = 5–20% by using the equation $\tau = \dfrac{1}{2\pi f_p}$ according to the relaxation peak position (f_p) on ε''. These dielectric responses, with their fittings (capacitance |C| and Bode drawings in Figure S20) by taking grain boundary contributions into account, are related to structurally heterogeneous contributions from the grain and grain boundary regions[30] as suggested by the impedance measurements (S19), which yields grain resistivities of 64 kΩ.cm, 23 kΩ.cm, 12 kΩ.cm and

14 kΩ.cm for the lepidocrocite-type titanates with R_{Fe} = 5–20%, while the resistivities for the grain boundaries are all beyond 10 MΩ, at least three orders of magnitude higher than that of the corresponding grains.

To gain insight into the underlying polarization mechanism, temperature-dependent conductivities (ln σ_g) were also recorded. Figure 5b summarizes the variations in ln σ_g vs. 1/T over the measured temperature region, which all show a well-defined linear characteristic in Arrhenius law[29]. Fitting the ln σ_g plots gives the activation energies (E_a) of 0.81, 0.73, 0.57, and 0.64 eV for the lepidocrocite-type titanates with R_{Fe} = 5–20%. Obviously, the lepidocrocite-type titanate of R_{Fe} = 15% possesses the smallest E_a, which can be associated with the optimum dielectric permittivity that will be addressed later. Further, M''/M''$_{max}$ combining with tanδ/tanδ_{max}, an effective approach, was employed to determine the dynamic nature of polaronic particles. It is well-established that, the peak positions of the two curves for a delocalized or long-range transport must be overlapped[31,32]. Figure 5c clearly suggests a localized or short-range character for the polaronic particles as the peak position of the M''/M''$_{max}$ and tanδ/tanδ_{max} curves is apparently not overlapped.

Discussion

Structural evolution by TiO$_6$ octahedral modification. TiO$_2$ (anatase, rutile and brookite) and lepidocrocite-type titanate are constructed of basic TiO$_6$ octahedral structural units. Previous work suggests that TiO$_2$ formation involves an intermediate titanate state followed by a deionization (e.g. Na$^+$ and/or H$^+$ ions) process[22,33]. Cations/anions during solution chemistry greatly affect surface charges and tensions, which in turn promote releasing Na$^+$/H$^+$ from titanate precursor to form TiO$_6$ octahedra and further enable TiO$_6$ octahedral reconstruction in terms of edge/vertex sharing to form brookite, anatase or rutile[33–35]. These TiO$_6$ octahedral units themselves are structurally distorted, and further become highly polarized when interacting with cations/anions, resulting in reconfigurations and reconnections in the solution reactions.

Generally, introducing heteroatom doping will affect the surrounding solution around heteroatom-containing TiO$_6$ octahedra while resulting in defect states that could change the polarity of the TiO$_6$ octahedra. The driving forces of the TiO$_6$ octahedra control are closely related to the degree of tolerance of the defects for TiO$_6$ octahedra in different crystalline polymorphs, which is intrinsically
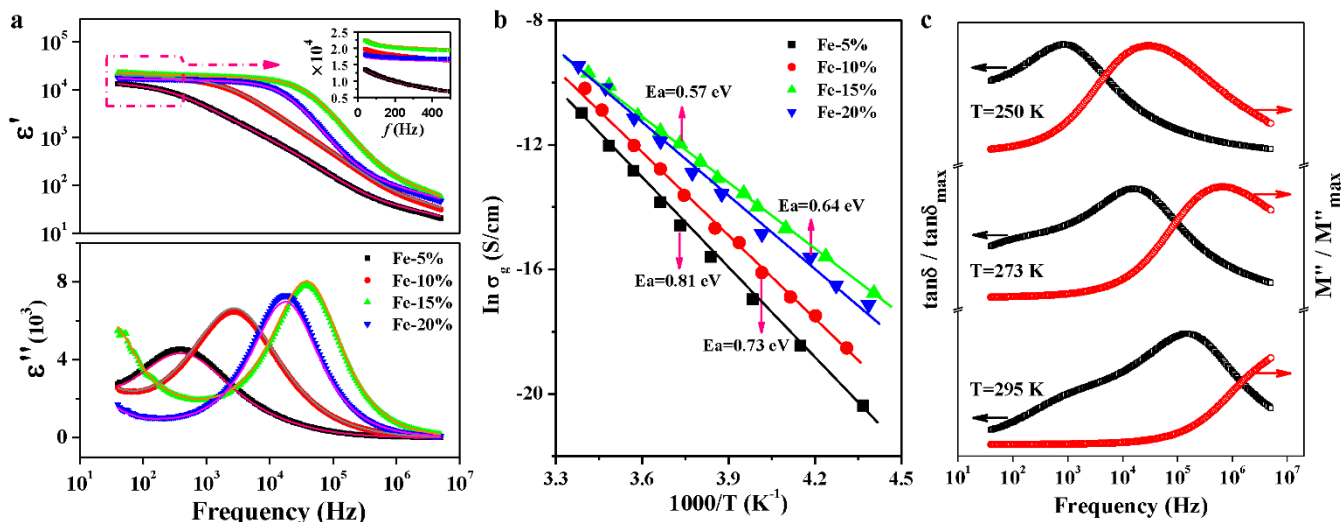
Figure 5 | Dielectric characterizations for Fe^{3+} doped lepidocrocite-type titanates with varying R_{Fe}. (a) Frequency dependences of dielectric permittivities (real part ε′ and imaginary part ε″) measured at room temperature as well as the fitting curves (solid lines). (b) Arrhenius plots of grain conductivities (ln σ_g) versus measured temperatures (1/T). Solid lines denote the fitting results using Arrhenius law $\ln(\sigma) = \frac{-E_a}{k_B}\left(\frac{1}{T}\right) + \ln \sigma_0$, where E_a is the activation energy, k_B the Boltzmann constant, σ_0 a constant related to the density of charge carriers and T the absolute temperature. Fitting the plots yields the E_a for lepidocrocite-type titanates with R_{Fe} = 5–20%. (c) Frequency dependences of normalized peaks, $\tan\delta/\tan\delta_{max}$ and M''/M''_{max} of lepidocrocite-type titanates with R_{Fe} = 5% at given temperatures.

linked to the local environment of the Ti atoms, as well as the types of introduced interfering ions.

Brookite→Anatase. The TiO_2 phase transformation from brookite to anatase promoted by the interfering Fe^{3+} ions can be ascribed to the differing structural arrangements of TiO_6 octahedra between brookite and anatase. TiO_6 octahedra in the anatase share edges along all three directions in a zigzag manner, while in the brookite, they become more complicated: TiO_6 octahedra only share edges along the *c* direction, but alternately share vertices and edges along both *a* and *b* directions (Figures 1a, 6). When trivalent iron ions (Fe^{3+}) are substitutionally doped into TiO_2, defect states such as oxygen vacancies should be spontaneously introduced to maintain charge neutrality[36]. Meanwhile, the octahedra become highly distorted and polarized, which results in local fluctuations in structure and energy. Thus, sharing one more O atom (*i.e.*, sharing two O atoms totally)
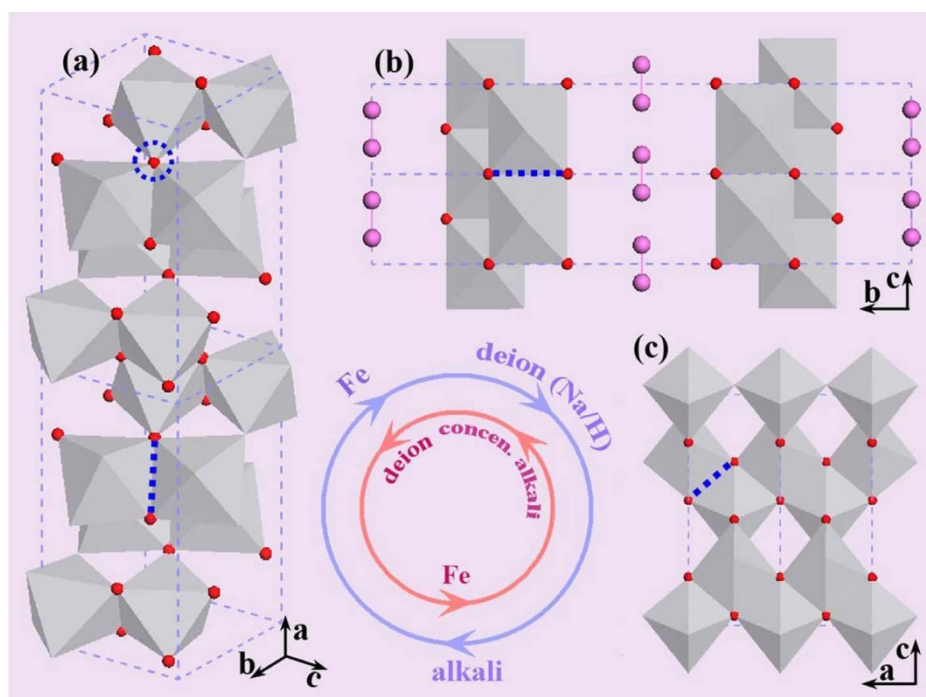

Figure 6 | Schematic representations of the structural evolutions with varying the TiO_6 octahedral connectivity and configuration. (a) brookite TiO_2. (b) lepidocrocite titanate. (c) anatase TiO_2. Two rings denote the reversible circles of phase transformation, and the corresponding directions are marked by arrows. The blue dashed ring and lines denote the vertex-sharing and edge-sharing connections of TiO_6 octahedra, respectively.

with the neighboring TiO_6 octahedron would be a better way to accomplish the defect compensation for the octahedra with Fe^{3+} situated, *i.e.*, through edge-sharing connections. Once the edge-sharing connection for two octahedra happens, local fluctuations around the octahedra with Fe^{3+} situated in the solution would favor edge-sharing connections for more octahedra to develop into the three-dimensional anatase nanostructures. This statement complies well with the predictions made by density functional theory (DFT) using the generalized gradient approximation taking into account the Hubbard level (GGA+U)[37,38], where convincing evidence that the presence of Fe^{3+} could strongly reduce the formation energy of defect states for anatase is provided. As a result, the TiO_6 octahedra involving Fe^{3+} ions, in order to tolerate the defect states, will restack and turn themselves into anatase from brookite. An indirect evidence for DFT prediction is that interfering Fe^{3+} ions result in band-gap narrowing, in good agreement with experimental results (S21). The TiO_6 octahedral modification with the phase evolution from brookite to anatase in the solution seems not obeying traditional crystal chemical theory where edge-sharing connection generally leads to cation-cation repulsions and then structural destabilization[39]. In fact, this is because the interfering Fe^{3+} ions play the key role in TiO_6 octahedra modification, which allows a better tolerance of defect states in anatase. Perhaps this is why it is so difficult to synthesize high-quality brookite. We have not found any report to date to successfully introduce dopant ions into brookite structure.

Brookite→Titanate. The crystal structure of lepidocrocite-type titanate consists of two-dimensional corrugated skeleton layers of edge- and corner-sharing TiO_6 octahedra (Figures 1a, 6c). The six Ti–O bonds in an octahedron can be classified into 3 pairs, since each pair in opposite directions has same length (Figures 1a, 3b). To this, the polarity (or symmetry) of the octahedra for lepidocrocite-type titanate should be lower (higher) than that for brookite but higher (lower) than that for anatase, since in brookite the lengths of six Ti–O bonds are all different, while in anatase four of them are short and two of them are long (Figure 1a)[9]. The substitutional Fe^{3+} ions, combined with those defects induced by interfering Fe^{3+} ions, further intensify the polarity and distortions of the TiO_6 octahedra. When the concentrations of OH^- and Na^+ ions in the solution are high enough, those TiO_6 octahedra would need to slightly rotate and change the lengths of the Ti–O bonds to release the local strain, because: (i) lepidocrocite-type titanate has a relatively high similarity to brookite in TiO_6 octahedral connectivity, which allows the control to be easily accomplished with only a small variation in energy; and (ii) OH^- and Na^+ ions, as well as protons (H^+ and/or $[H_3O]^+$) in the solution can bond to the TiO_6 octahedra to compensate the charge neutrality and minimize the lattice relaxation, further stabilizing the octahedral skeletons. For lepidocrocite-type titanate, interlayer confined ions (Na^+ ions and protons) are weakly bonded to the Ti-O skeletons, which are thus sufficiently flexible to be even altered and replaced[27]. When heterovalent Fe^{3+} ions were introduced, layer-structured titanate can tune the interlayer spacing to compensate for both the defect states and host-guest mismatching that are induced by the substitution of Fe^{3+} for Ti^{4+}, accompanied with the accommodation of more Na^+ ions and protons (H^+ and/or $[H_3O]^+$) into the interlayers, for charge balance and TiO_6 octahedral skeleton stabilization. This is why the contents of Na^+ ions and the hydrated groups are slightly increased with increasing R_{Fe} as indicated by ICP and TG. By contrast, for brookite TiO_2, due to the absence of lattice Na^+/H^+ ions, charge neutrality can only be compensated by those defect states (*e.g.* vacancies), spontaneously leading to structural instability for the Ti–O networks and thus recombination of TiO_6 octahedra[10,40].

Nanotube→Nanosheet (titanate). Previous studies on several types of titanates indicate that a layered crystal structure is an important prerequisite for nanotube formation[41]. Differently, the formation of doped lepidocrocite-type titanate nanotubes here is a consequence of the interfering ions (Fe^{3+}) that play a key role in TiO_6 octahedral modification. Substitution of Ti^{4+} with the smaller-size and lower-valent Fe^{3+} gives rise to charge imbalance as well as internal strain in the TiO_6 octahedra, and even bending of Ti–O skeleton layers in order to compensate the elevated surface tension and free energy[42,43]. However, when R_{Fe} is relatively high, the TiO_6 octahedra cannot accommodate so many Fe^{3+} counterparts and defect states. As a result, partial Fe^{3+} ions are situated at the interlayer sites of the original Na^+ species. Since these Fe^{3+} ions are much smaller in size than that of the interlayered Na^+ species, the spacing of the interlayer would slightly reduce, somewhat like the protonated sodium titanate after acid rinsing[20]. At this stage, the electrical repulsive interaction between two Ti–O skeleton layers would dramatically accelerate to produce relatively high Coulomb repulsive energy, which directly results in layered structure collapse as indicated by a theoretical study[43]. The occupational competition between the skeletal Fe^{3+} and the interlayered Fe^{3+} allows lepidocrocite-type titanate nanotubes to completely convert into the nanosheets.

Associated with the TiO_6 octahedral control, the structurally mutual evolution between brookite, anatase, and lepidocrocite-type titanate can be achieved through appropriately controlling the synthetic conditions of solution chemistries. The TiO_6 octahedra in the as-prepared lepidocrocite-type titanates could be modified in the solution reactions and convert to anatase or brookite by deionizing, *i.e.*, releasing Na^+ (and/or doped Fe^{3+}) species and protons (S22), which has been accepted as an important route for TiO_2 synthesis.[35] Conversely, Ti–O bonds in TiO_2, as indicated from previous work, could react with the concentrated alkali, leading to lamellar fragments of Ti–O frameworks, and finally reconstruct into titanates[43,44]. In summary, the mutual evolution between TiO_2 and lepidocrocite-type titanate is the result of TiO_6 octahedral modification, which can be well controlled in solution chemistries, as schematically demonstrated in Figure 6.

TiO_6 octahedral modification for optimum giant dielectric response. Microstructure- and morphology-related physical and chemical properties of solids are of significant importance in fabricating functional nanostructures[45]. The dielectric properties of nano-based materials could be directly related to the microstructure of the solid, *i.e.* the nanoscale bulk and interfaces, where the solid can be defective or even polarized as a result of surface defect dipoles and/ or surface charges, which are expected to be even larger when heteroatoms are involved. Earlier structural analysis identified that substitutional Fe^{3+} ions greatly influence the local environment and polarity of TiO_6 octahedra thereby altering the macroscopic morphology. Since Fe^{3+} is slightly smaller in both size and valence than Ti^{4+}, substitution of Fe^{3+} for Ti^{4+} would force local shrinkage of the lattice, resulting in local strain across a few atomic distances. Meanwhile, local disorder/distortion surrounding the Fe^{3+} will also appear due to dopant-host mismatching like many other doping cases[46,47]. That is, introducing Fe^{3+} could cause a local charge imbalance, leading to a polaronic-like distortion[31]. As a result, defect dipoles induced by *e.g.* ion-defect pairs, local defects or distortion would form to act as the available polaronic species, making a contribution to the high dielectric permittivity observed[8,30,48]. These defect dipoles, with short-range behaviour, are unable to catch up with the oscillation of the externally applied electric field, causing a quick decrease in ε' at relatively high frequencies. Apparently, the number of these defect dipoles is proportional to R_{Fe} and its transport nature is determined by R_{Fe}, *i.e.*, intrinsically linked to the TiO_6 octahedral modification and microstructural nature.

It is well established that the transformation from lepidocrocite-type titanate nanotubes to nanosheets is a result of TiO_6 octahedral control caused by the incorporation of interfering Fe^{3+} ions. Here,

R_{Fe} has two impacts: one is an increase in the number of defect dipoles and the other is that hydrated groups (associated with protons, H^+ and/or $[H_3O]^+$, etc.) and heavy Fe^{3+} instead of Na^+ ions are partially dispatched into the interlayers. Our previous study indicates that inter-layered Na^+ ions in sodium titanate nanotubes can easily migrate to induce charges at the interfaces, and the conductivity of sodium-rich lepidocrocite-type titanate is one or two orders of magnitude higher than that of the protonated lepidocrocite-type titanate with more hydrated groups[44]. Thus, inter-layered Na^+ ions in Fe^{3+}-doped lepidocrocite-type titanates would not be expected to hinder the polaronic transport. Comparatively, hydrated groups are strongly bonded to TiO_6 octahedral skeleton layers, and meanwhile Fe^{3+} is too heavy to migrate, both of which thus act as a giant barrier to obstruct the polaronic transport[49]. Consequently, the competition of the above two aspects gives rise to the shortest τ, smallest grain σ_g and E_a, responsible for the optimum dielectric property. It should be noted that the giant dielectric response is not related to those space charges induced by the electronic hopping from possibly delocalized $3d^1$ of Ti^{3+} as there is no trace of Ti^{3+} detected by EPR (Figure 2c) and XPS (S23).

The primary goal of this work is to establish the structure/property correlation via atomic-scale control over the connectivity and configurations of TiO_6 octahedra through solution chemistry. Further, when taking into consideration the fact that nearly all of the metal-oxide materials obtained are constructed by metal-oxygen polyhedral (MO_n) units, one can envisage atomic-scale reaction mechanisms for synthesizing metal-oxide nanostructures, which is expected to remain an important and exciting subject for future studies, a judicious choice that enables simple bottom-up fabrication of structurally more complex metal-oxides or multifunctional materials and devices.

Methods

Sample Preparation. The synthesis of titanium-based oxide nanostructures was performed by solution chemistry using the following procedure: 0.04 mol $TiOSO_4$ (Ourchem, 99%) was dissolved into 100 mL deionized water to form solution (I). 0.025 mol NaOH (Sinoreagent, 99.9%) was dissolved into 100 mL deionized water to form solution (II). Subsequently, solution (I) was slowly added into solution (II) while stirring. The resultant white suspension was thoroughly filtered and then dispersed in water to form a precursor solution through magnetic-ultrasonic stirring for 12 h. 2 M NaOH or H_2SO_4 (Sinoreagent, 99.9%) solution was then added to adjust the pH value. The resultant precursor solutions were then sealed in Teflon-lined stainless steel autoclaves and reacted at 220°C for 48 h for precipitation and crystallisation. The reaction products were filtered, washed with distilled water, and dried in air to get the final samples.

Using a similar synthesis procedure, interfering Fe^{3+} ions (also the Sc^{3+} and Sm^{3+} ions for investigating the effects from different sizes of interfering ions), were then incorporated into the titanium-based oxide nanostructures to control the configurations and connectivity of the TiO_6 octahedral units in an attempt to control the microstructures and properties of the resultant Ti-based oxides. The Fe^{3+}-doped titanium-based nanostructures were achieved via the dissolution of the appropriate relative amount of $TiOSO_4$ and $Fe_2(SO_4)_3$ (Sinoreagent, 99.9%) into 100 mL of deionized water to give a total mole amount of 0.04 with mole ratios $R_{Fe} = Fe/(Fe + Ti)$ with values of 5%, 10%, 15%, and 20%, respectively. The remaining synthesis procedures were the same as outlined above for the un-doped titanium-based nanostructures. The preparation procedure of titanium-based nanostructures with doping other interfering ions i.e. Sc^{3+} and Sm^{3+} is similar to the case of Fe^{3+}.

Sample Characterizations. The chemical compositions of the resultant samples were determined by inductively coupled plasma-atomic emission spectrometry (ICP-AES). The phase purity and crystallinity of the samples were characterised by X-ray diffraction (XRD, Rigaku Dmax2500, Cu $K\alpha$ radiation, $\lambda = 0.15418$ nm). Ni powders were chosen as an internal standard for the determination of the peak positions. The average crystallite size, D, was calculated via the Scherrer formula, $D = 0.9\lambda/(\beta\cos\theta)$, where λ is the X-ray wavelength employed, θ is the diffraction angle and β is defined as the half width after subtracting instrumental broadening. Structural refinements on the XRD patterns were performed using the Rietveld method. The particle size, morphology, and microstructures of the samples were characterized using field emission scanning electron microscopy (SEM, JEOL JSM-6700), transmission electron microscopy (TEM, JEOL JEM-2010). Energy-dispersive X-ray spectroscopy (EDS) data were collected on INCA Energy 450 EDXA system.

Optical diffuse reflectance spectra of the samples were collected at room temperature via a Lambda 900 UV-vis spectrometer. Raman spectra of the final products were obtained on a UV-vis Raman System (Renishaw 1000) with an excitation

wavelength of 532 nm. Their infrared optical spectra were also collected by a Perkin-Elmer IR spectrophotometer. Thermal analysis of the samples was performed by thermogravimetric (TG) analysis (Netzsch STA449C). The valence and defect states were studied by X-ray photoelectron spectroscopy (XPS, ESCA-LAB MKII spectrometer) and electron paramagnetic resonance (EPR, Bruker BioSpin EPR) at a microwave frequency of 9.86 GHz.

Electrical and dielectric measurements. The samples were also hot-pressed at a pressure of 12 MPa at 200°C for 30 min to make pellets with a diameter/thickness of 12/1.5 mm. Both sides of the pellets were then coated with Ag-based conductive electrodes and dried under infrared radiation. Alternative current (AC) impedance measurements were carried out using a precision LCR meter (Agilent 4294A) over a frequency (f) range from 40 Hz to 5 MHz at selected temperatures to obtain the complex impedance $Z*(\omega) = Z'(\omega) - iZ''(\omega)$, where $Z'(\omega)$ and $Z''(\omega)$ are real and imaginary parts, respectively. The complex dielectric permittivity $\varepsilon*(\omega)$ was then extracted based on the relation $\varepsilon*(\omega) = \varepsilon'(\omega) - i\varepsilon''(\omega) = \frac{1}{i\omega C_0 Z*(\omega)}$, where $\omega(=2\pi f)$ is the angular frequency and $C_0 = \varepsilon_0 S/L$ represents the vacuum capacitance of a capacitor with an area of S and a thickness of L. These impedance parameters were also modeled using the least-squares refinement program EQUIVCRT to obtain an equivalent circuit through which the equivalent grain and grain boundary conductivity can be deduced.

1. Satoh, N., Nakashima, T. & Yamamoto, K. Metastability of anatase: size dependent and irreversible anatase-rutile phase transition in atomic-level precise titania. *Sci. Rep.* **3**, 1959 (2013).
2. Rondinelli, J. M., May, S. J. & Freeland, J. W. Control of octahedral connectivity in perovskite oxide heterostructures: An emerging route to multifunctional materials discovery. *MRS Bulletin* **37**, 261–270 (2012).
3. Ju, L. et al. Interplay between Size, Composition, and Phase Transition of Nanocrystalline Cr^{3+}-Doped $BaTiO_3$ as a Path to Multiferroism in Perovskite-Type Oxides. *J. Am. Chem. Soc.* **134**, 1136–1146 (2012).
4. Ren, Z. et al. $PbTiO_3$ Nanofibers with Edge-Shared TiO_6 Octahedra. *J. Am. Chem. Soc.* **132**, 5572–5573 (2010).
5. Liu, S. et al. Synthesis of chiral TiO_2 nanofibre with electron transition-based optical activity. *Nat. Commun.* **3**, 1215 (2012).
6. Wang, Y. et al. Role of point defects on the reactivity of reconstructed anatase titanium dioxide (001) surface. *Nat. Commun.* **4**, 2214 (2013).
7. Wu, W.-Q. et al. Maximizing omnidirectional light harvesting in metal oxide hyperbranched array architectures. *Nat. Commun.* **5**, 3968 (2014).
8. Hu, W. et al. Electron-pinned defect-dipoles for high-performance colossal permittivity materials. *Nat. Mater.* **12**, 821–826 (2013).
9. Gong, X.-Q. & Selloni, A. First-principles study of the structures and energetics of stoichiometric brookite TiO_2 surfaces. *Phys. Rev. B* **76**, 235307 (2007).
10. Wang, X. H. et al. Pyrogenic Iron(III)-doped TiO_2 nanopowders synthesized in RF thermal plasma: Phase formation, defect structure, band gap, and magnetic properties. *J. Am. Chem. Soc.* **127**, 10982–10990 (2005).
11. Aimi, A. et al. High-Pressure Synthesis of A-Site Ordered Double Perovskite $CaMnTi_2O_6$ and Ferroelectricity Driven by Coupling of A-Site Ordering and the Second-Order Jahn-Teller Effect. *Chem. Mater.* **26**, 2601–2608 (2014).
12. Aso, R., Kan, D., Shimakawa, Y. & Kurata, H. Atomic level observation of octahedral distortions at the perovskite oxide heterointerface. *Sci. Rep.* **3**, 2214 (2013).
13. Neagu, D., Tsekouras, G., Miller, D. N., Menard, H. & Irvine, J. T. S. In situ growth of nanoparticles through control of non-stoichiometry. *Nature Chem.* **5**, 916–923 (2013).
14. Fabregat-Santiago, F. et al. High carrier density and capacitance in TiO_2 nanotube arrays induced by electrochemical doping. *J. Am. Chem. Soc.* **130**, 11312–11316 (2008).
15. Gateshki, M., Yin, S., Ren, Y. & Petkov, V. Titania polymorphs by soft chemistry: Is there a common structural pattern? *Chem. Mater.* **19**, 2512–2518 (2007).
16. Barnard, A. S. & Curtiss, L. A. Prediction of TiO_2 nanoparticle phase and shape transitions controlled by surface chemistry. *Nano Lett.* **5**, 1261–1266 (2005).
17. Shah, S. I., Li, W., Huang, C. P., Jung, O. & Ni, C. Study of Nd^{3+}, Pd^{2+}, Pt^{4+}, and Fe^{3+} dopant effect on photoreactivity of TiO_2 nanoparticles. *Proc. Natl. Acad. Sci. U. S. A.* **99**, 6482–6486 (2002).
18. Fabrega, C., Andreu, T., Cabot, A. & Morante, J. R. Location and catalytic role of iron species in TiO_2: Fe photocatalysts: An EPR study. *J. Photochem. Photobiol. A* **211**, 170–175 (2010).
19. Sasaki, T. et al. Preparation and Acid-Base Properties of a Protonated Titanate with the Lepidocrocite-like Layer Structure. *Chem. Mater.* **7**, 1001–1007 (1995).
20. Mao, Y. B. & Wong, S. S. Size- and shape-dependent transformation of nanosized titanate into analogous anatase titania nanostructures. *J. Am. Chem. Soc.* **128**, 8217–8226 (2006).
21. Lin, H. et al. Synthesis of High-Quality Brookite TiO_2 Single-Crystalline Nanosheets with Specific Facets Exposed: Tuning Catalysts from Inert to Highly Reactive. *J. Am. Chem. Soc.* **134**, 8328–8331 (2012).
22. Hu, W., Li, L., Li, G., Tang, C. & Sun, L. High-Quality Brookite TiO_2 Flowers: Synthesis, Characterization, and Dielectric Performance. *Cryst. Growth Des.* **9**, 3676–3682 (2009).
23. Buonsanti, R. et al. Nonhydrolytic synthesis of high-quality anisotropically shaped brookite TiO_2 nanocrystals. *J. Am. Chem. Soc.* **130**, 11223–11233 (2008).

24. Bavykin, D. V., Friedrich, J. M. & Walsh, F. C. Protonated titanates and TiO$_2$ nanostructured materials: Synthesis, properties, and applications. *Adv. Mater.* **18**, 2807–2824 (2006).

25. Gao, T., Fjellvag, H. & Norby, P. Crystal Structures of Titanate Nanotubes: A Raman Scattering Study. *Inorg. Chem.* **48**, 1423–1432 (2009).

26. Shripal, Tandon, R. P. & Pandey, S. D. ectrical conductivity and EPR investigations in iron doped polycrystalline K$_2$Ti$_4$O$_9$. *J. Phys. Chem. Solids* **52**, 1101–1107 (1991).

27. Gao, T., Fjellvag, H. & Norby, P. Defect Chemistry of a Zinc-Doped Lepidocrocite Titanate Cs$_x$Ti$_{2-x/2}$Zn$_{x/2}$O$_4$ (x = 0.7) and its Protonic Form. *Chem. Mater.* **21**, 3503–3513 (2009).

28. Pecchi, G. *et al.* Effect of precursors on surface and catalytic properties of Fe/TiO$_2$ catalysts. *J. Chem. Technol. Biotechnol.* **77**, 944–949 (2002).

29. Jonscher, A. K. Dielectric relaxation in solids. *J. Phys. D-Appl. Phys.* **32**, R57–R70 (1999).

30. Guillemet-Fritsch, S. *et al.* Colossal permittivity in ultrafine grain size BaTiO$_{3-x}$ and Ba$_{0.95}$La$_{0.05}$TiO$_{3-x}$ materials. *Adv. Mater.* **20**, 551–555 (2008).

31. Dutta, A., Sinha, T. P. & Shannigrahi, S. Dielectric relaxation and electronic structure of Ca(Fe$_{1/2}$Sb$_{1/2}$)O$_3$. *Phys. Rev. B* **76**, 155113 (2007).

32. Gerhardt, R. Impedance and dielectric spectroscopy revisited: Distinguishing localized relaxation from long-range conductivity. *J. Phys. Chem. Solids* **55**, 1491–1506 (1994).

33. Nagase, T. *et al.* Hydrothermal synthesis of brookite. *Chem. Lett.* 911–912 (1999).

34. Deng, Q. *et al.* Selective Synthesis of Rutile, Anatase, and Brookite Nanorods by a Hydrothermal Route. *Curr. Nanosci.* **6**, 479–482 (2010).

35. Zhu, H. Y. *et al.* Phase transition between nanostructures of titanate and titanium dioxides via simple wet-chemical reactions. *J. Am. Chem. Soc.* **127**, 6730–6736 (2005).

36. Wu, Q. & van de Krol, R. Selective Photoreduction of Nitric Oxide to Nitrogen by Nanostructured TiO$_2$ Photocatalysts: Role of Oxygen Vacancies and Iron Dopant. *J. Am. Chem. Soc.* **134**, 9369–9375 (2012).

37. Roldan, A., Boronat, M., Corma, A. & Illas, F. Theoretical Confirmation of the Enhanced Facility to Increase Oxygen Vacancy Concentration in TiO$_2$ by Iron Doping. *J. Phys. Chem. C* **114**, 6511–6517 (2010).

38. Shao, G. Red Shift in Manganese- and Iron-Doped TiO$_2$: A DFT+U Analysis. *J. Phys. Chem. C* **113**, 6800–6808 (2009).

39. Gibbs, G. V. & Smith, J. V. Refinement of the crystal structure of synthetic pyrope. *Am. Mineral.* **50**, 2023–2039 (1965).

40. Gennari, F. C. & Pasquevich, D. M. Kinetics of the anatase rutile transformation in TiO$_2$ in the presence of Fe$_2$O$_3$. *J. Mater. Sci.* **33**, 1571–1578 (1998).

41. Hu, W., Li, L., Tong, W. & Li, G. Water-titanate intercalated nanotubes: fabrication, polarization, and giant dielectric property. *Phys. Chem. Chem. Phys.* **12**, 12638–12646 (2010).

42. Zhang, S. *et al.* Formation mechanism of H$_2$Ti$_3$O$_7$ nanotubes. *Phys. Rev. Lett.* **91**, 256103 (2003).

43. Zhang, S., Chen, Q. & Peng, L. M. Structure and formation of H$_2$Ti$_3$O$_7$ nanotubes in an alkali environment. *Phys. Rev. B* **71**, 014104 (2005).

44. Hu, W., Li, L., Li, G., Meng, J. & Tong, W. Synthesis of Titanate-Based Nanotubes for One-Dimensionally Confined Electrical Properties. *J. Phys. Chem. C* **113**, 16996–17001 (2009).

45. Chung, U. C. *et al.* Interface Investigation in Nanostructured BaTiO$_3$/Silica Composite Ceramics. *J. Am. Ceram. Soc.* **93**, 865–874 (2010).

46. Yalcin, Y., Kilic, M. & Cinar, Z. Fe^{+3}-doped TiO$_2$: A combined experimental and computational approach to the evaluation of visible light activity. *Appl. Catal. B* **99**, 469–477 (2010).

47. Al-Harthi, S. *et al.* Structural analysis and band gap tailoring of Fe^{3+}-doped Zn-TiO$_2$ nanoparticles. *Appl. Phys. A: Mater. Sci. Process.* **99**, 237–244 (2010).

48. Thongbai, P., Tangwancharoen, S., Yamwong, T. & Maensiri, S. Dielectric relaxation and dielectric response mechanism in (Li, Ti)-doped NiO ceramics. *J. Phys.:Condens. Matter* **20**, 395227 (2008).

49. Lin, Y., Shiomi, J., Maruyama, S. & Amberg, G. Dielectric relaxation of water inside a single-walled carbon nanotube. *Phys. Rev. B* **80**, 045419 (2009).

Acknowledgments

Author contributions

W.H., L.L., G.S., Y.L. and R.L.W. contributed to the preparation of manuscript, and involved in all discussions regarding the data interpretations, and structural analysis. G.L. and L.L. initiated the study and coordinate various experimental works. W.H. fabricated the samples with different synthesizing conditions, and conducted the characterizations (XRD, SEM, SEM-EDS, TEM, Raman, FT-IR, UV-vis, TG, EPR, XPS) and electrical properties.

Additional information

Supplementary information accompanies this paper at http://www.nature.com/scientificreports

Competing financial interests: The authors declare no competing financial interests.

How to cite this article: Hu, W., Li, L., Li, G., Liu, Y. & Withers, R.L. Atomic-scale control of TiO$_6$ octahedra through solution chemistry towards giant dielectric response. *Sci. Rep.* **4**, 6582; DOI:10.1038/srep06582 (2014).